Observation of Brownian Motion in Liquids at Short Times: Instantaneous Velocity and Memory Loss
Simon Kheifets *et al.*
Science **343**, 1493 (2014);
DOI: 10.1126/science.1248091

Observation of Brownian Motion in Liquids at Short Times: Instantaneous Velocity and Memory Loss

Simon Kheifets, Akarsh Simha, Kevin Melin, Tongcang Li,* Mark G. Raizen†

Measurement of the instantaneous velocity of Brownian motion of suspended particles in liquid probes the microscopic foundations of statistical mechanics in soft condensed matter. However, instantaneous velocity has eluded experimental observation for more than a century since Einstein's prediction of the small length and time scales involved. We report shot-noise–limited, high-bandwidth measurements of Brownian motion of micrometer-sized beads suspended in water and acetone by an optical tweezer. We observe the hydrodynamic instantaneous velocity of Brownian motion in a liquid, which follows a modified energy equipartition theorem that accounts for the kinetic energy of the fluid displaced by the moving bead. We also observe an anticorrelated thermal force, which is conventionally assumed to be uncorrelated.

Einstein's seminal work on Brownian motion introduced a quantitative description of diffusion at long time scales (1). It led to experimental evidence of the molecular theory of matter and also explained why measurements of the velocity of Brownian particles were inconsistent with the equipartition theorem, a fundamental prediction of statistical mechanics (2, 3). Einstein considered the average velocity $\bar{v}_\tau$ measured over time interval τ. For diffusive Brownian motion, his theory predicted a root-mean-square value of $\bar{v}_\tau$ proportional to $\tau^{-1/2}$, diverging as τ approaches zero (4, 5). Einstein estimated that his simplification would break down at time scales on the order of τ_p, the momentum relaxation time. He claimed that the direct observation of the microscopic statistical mechanics of the Brownian particle, through measurement of the instantaneous velocity, would be "impossible" due to the demands on spatial and temporal resolution (4). A larger particle relaxes the demands on temporal resolution, but increases demands on position resolution owing to its slower thermal velocity. Recent work reported measurement of the instantaneous velocity of a Brownian particle in air, leading to confirmation of the equipartition theorem (5), providing access to dynamics otherwise concealed by thermal averaging (6), and allowing active suppression of thermal fluctuations (7). Velocity measurement in air was facilitated by advances in ultrasensitive detection and by the larger value of τ_p that results from the lower viscosity of air compared to liquid (5). In liquids, hydrodynamic coupling between the bead and the fluid dominates the dynamics of velocity fluctuations, whereas in air it is negligible. It is now understood that this coupling is important to both the fundamental statistics of Brownian fluctuations (8, 9) and to dynamics at time scales relevant to biological

systems (10), colloidal systems (11), and microfluidics (12).

Previous experiments reported observation of time-averaged hydrodynamic effects in Brownian motion for times as short as $\tau_f/15$, where τ_f is the time scale of bead-fluid interaction (13, 14). However, interesting effects of hydrodynamic interaction also extend to times that are orders of magnitude shorter than τ_f, while time-averaging imposes a thermal distribution of initial velocities and conceals the onset of equilibrium. In this work, we track the Brownian motion of dielectric microspheres (silica and barium titanate glass) suspended by an optical tweezer in water and acetone (Fig. 1). We achieve shot-noise–limited position sensitivity below 3 fm/$\sqrt{\text{Hz}}$ with a bandwidth of more than 50 MHz, which, combined

with an appropriate choice of system parameters, allows us to observe single-particle dynamics at times as short as $\tau_f/300$ and to resolve the Brownian particles' instantaneous velocity.

In Einstein's picture, mean-squared displacement (MSD) of Brownian trajectories is described by the diffusion equation, $\text{MSD}(\tau) \equiv \langle [\Delta x(\tau)]^2 \rangle = 2D\tau$ where D is the diffusion constant. Because of their fractal nature, purely diffusive trajectories have infinite length and thus an undefined instantaneous velocity, in contradiction of the equipartition theorem (5). This contradiction is resolved when the inertial mass of the particle is taken into account. Such a solution can be found by solving the stochastic Langevin equation, $m_p\dot{v} = F_{fr}(v) + F_{th}(t)$ where m_p is the mass of the particle, v is its velocity, $F_{fr}(v)$ is the damping force due to the fluid, and $F_{th}(t)$ is a random thermal force. The Langevin equation can be solved for the MSD and the corresponding velocity autocorrelation function $\text{VACF}(\tau) \equiv \langle v(t)v(t + \tau) \rangle = d^2/d\tau^2(\text{MSD}(\tau)/2)$. The solution requires knowledge of the autocorrelation of the thermal force which, by the fluctuation dissipation theorem, can be determined from the dissipative component of F_{fr} (15).

The simplest model of ballistic Brownian motion assumes Stokes damping, $F_{fr} = -\gamma_s v$ with Stokes drag coefficient $\gamma_s = 6\pi\eta r$ for a spherical particle of radius r in a fluid with dynamic viscosity η. The resulting solution is characterized by an exponentially decaying VACF, with time-constant $\tau_p = m_p/\gamma_s$ (16). At long times, the model reduces to diffusive motion, whereas at short times, the MSD is proportional to τ^2, and the VACF approaches its asymptotic value of $\langle v^2 \rangle = k_B T/m$, where k_B is Boltzmann's constant
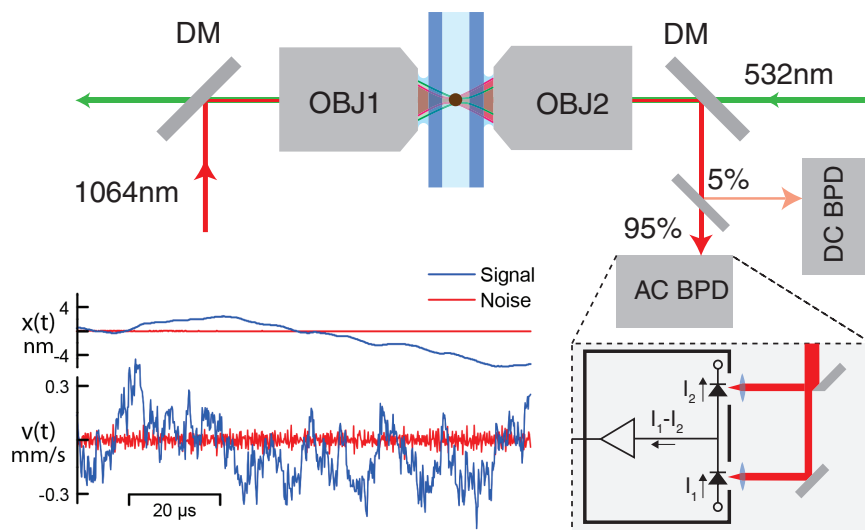
Fig. 1. A simplified schematic of the optical trap and position detection system. A microsphere is trapped by counterpropagating 1064- and 532-nm laser beams focused by microscope objectives (OBJ). The 1064-nm laser is then used to detect the horizontal motion of the bead, split between a low-power, dc balanced photodetector (DC BPD) and a high-power, ac-coupled balanced photodetector (AC BPD) (DM: dichroic mirror). Inset: A sample of the position (top trace) and velocity (bottom trace) of a trapped 3.7-μm-diameter barium titanate microsphere (blue line) recorded by the ac detector; the red line is the signal recorded with the same laser power but an empty trap.

Center for Nonlinear Dynamics and Department of Physics, University of Texas at Austin, Austin, TX 78712, USA.

*Present address: University of California, Berkeley, CA, USA.
†Corresponding author. E-mail: raizen@physics.utexas.edu

and T is the temperature, corresponding to the regime of ballistic motion. We refer to this solution as the Ornstein-Uhlenbeck model. Although Stokes damping holds for motion at constant velocity, two extra terms are required to correctly describe the force on a particle with nonzero acceleration.

In a dense fluid, the gravitational mass of an object is modified as a result of pressure from the fluid it displaces. Similarly, an object's inertial mass must be modified to account for the inertia of the displaced fluid. The effective particle mass is thus $m^* = m_p + m_a$, where, for a sphere in an unbounded fluid, the added (inertial) mass of the displaced fluid is $m_a = \frac{2}{3}\pi r^3 \rho_f$ (17), which is non-negligible when fluid density (ρ_f) is comparable to that of the particle (ρ_p). The equipartition prediction for the mean-squared thermal velocity of the hydrodynamically coupled bead is thus $\langle v_{th}^{2*}\rangle \equiv k_B T/m^*$ for each Cartesian component of the velocity.

In a viscous fluid, memory of the acceleration of a sphere at one instant is retained by vorticity in the fluid flow. Vorticity is generated at the sphere's surface and gradually expands outwards, affecting the force on the sphere at later times. The difference between this dynamic force and steady-state Stokes damping is known as the Basset force (18, 19):

$$F_B(t) = -\gamma_s \sqrt{\frac{\tau_f}{\pi}} \int_{-\infty}^{t} \frac{\dot{v}(t')}{\sqrt{t-t'}} dt' \qquad (1)$$

where $\tau_f = r^2 \rho_f / \eta$ is the time over which the vorticity expands a distance r, and $\dot{v}$ is the acceleration. The Basset force is not purely dissipative; energy from the entrained fluid can be returned to the particle. For short-time velocity fluctuations, the Basset force can dominate Stokes damping (fig. S3D), whereas for long-time fluc-

tuations it can dominate inertial forces (fig. S3C). At intermediate times it can dominate both. This behavior can be illustrated by considering the force required to accelerate an initially stationary sphere, $v(t < 0) = 0$ with constant acceleration at time $t = 0$, $\dot{v}(t \geq 0) = a_0$. The contribution by the Basset force grows as $t^{1/2}$, surpassing the inertial force $-m_a a_0$ of the added mass at $t \approx \tau_f/100$ and dominating the Stokes damping force $-\gamma_s a_0 t$ until $t \approx \tau_f$. Addition of the Basset force to the Langevin equation requires modification of the statistics of the random thermal force, substantially changes the behavior of the VACF (20, 21), and could potentially cause deviation from a Gaussian velocity distribution (9).

Figure 1 shows a simplified schematic of our experiment. An optical tweezer is created by two counterpropagating laser beams (1064 and 532 nm, both ~200 mW) focused by two identical water-immersion microscope objectives (numerical aperture 1.23). A flow-cell between the two objectives is used to introduce particles into the tweezer. The horizontal component of the trapped particle's displacement is measured with split-beam detection (5). The 1064-nm beam is split between two detectors, a high-power (~100 mW), low-noise ac-coupled detector (whose response is shown in fig. S1) and a low-power dc-coupled detector (22). The signals from each detector are digitized and stored on a computer. The particle diameter d, the trap constant K, and the detector calibration coefficient are determined by using a least-squares fit of the MSD of the recorded trajectories (Fig. 2A). All of the data used in this paper come from 0.35-s recorded trajectories of a barium titanate microsphere in acetone ($d = 3.72 \pm 0.06$ μm, $K = 3.2 \pm 0.2 \times 10^{-4}$ N/m, $\tau_f = 8.5$ μs) and a silica microsphere in water ($d = 2.86 \pm 0.03$ μm, $K = 1.6 \pm 0.3 \times 10^{-4}$ N/m, $\tau_f = 2.0$ μs).

The uncertainty of each fit parameter is determined from the variance in the results of independent MSD fits for 10 subtrajectories.

Our measured MSD and VACF demonstrate that we can observe dynamics deep into the ballistic regime. At short times, the MSD (Fig. 2A) has slope 2 (in a log-log plot), a signature of the ballistic regime of Brownian motion. The harmonic potential causes the MSD to plateau around $\tau_k \equiv \gamma_s/K$, before the purely diffusive regime is reached. The transition is more evident in the VACF (shown normalized by $\langle v_{th}^{2*}\rangle$ in Fig. 2B). At short times the VACF decays, to first order, as $1 - \sqrt{t/\tau_v}$, where $\tau_v = (\pi/4)(\tau_p^2/\tau_f)$ (22). This faster-than-exponential decay results from a two-fold action of the Basset force, which increases both the strength of the damping force and the magnitude of thermal force fluctuations at short time scales. The more familiar long-time tails (8, 23–25) appear at times longer than τ_f. The barium titanate microsphere in acetone has a much larger τ_v (11 μs) compared to the silica microsphere in water (0.57 μs), owing to the comparatively larger ρ_p of barium titanate and smaller ρ_f and η of acetone. The larger value of τ_v facilitates instantaneous-velocity measurement.
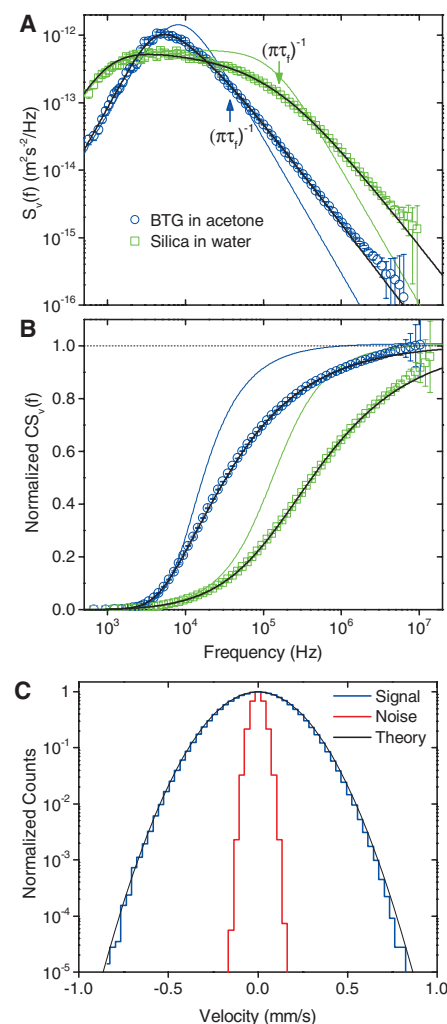
The useful bandwidth of instantaneous-velocity measurement is limited not directly by the detector bandwidth, but by the noise floor of the detector. The presence of shot noise in position measurement results in b^3 growth of the mean-square noise in velocity measurement, where b is the bandwidth chosen for measurement. Noise can be reduced by decreasing b, but if b is too low, the measured velocity will give a smaller apparent mean kinetic energy than the equipartition thermal energy $E_{th} \equiv k_B T/2$. The effect of low-pass filtering on the mean-square value of the resulting velocity can be estimated from the
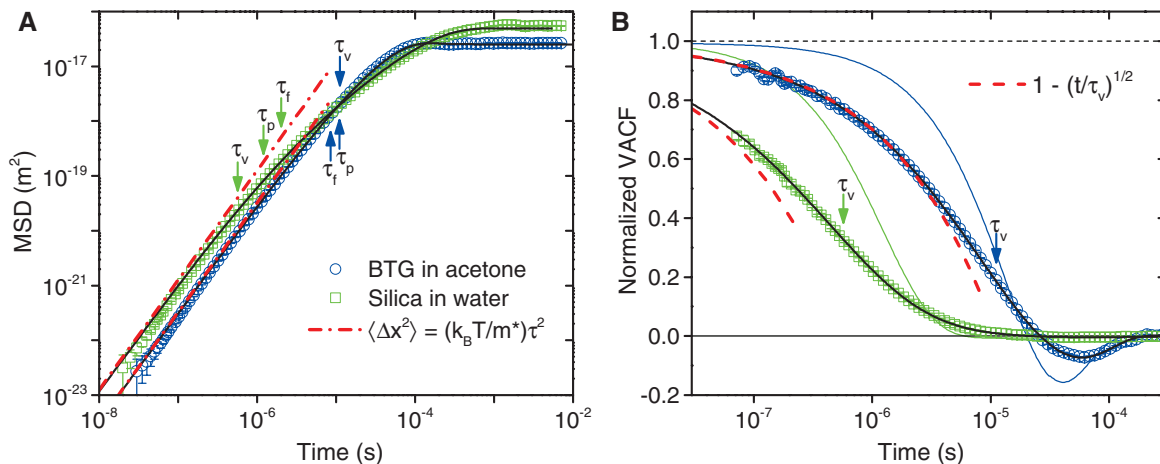
Fig. 2. Experimental and theoretical correlation functions from recorded trajectories of two different bead-fluid combinations. (**A**) Double-logarithmic plot of the MSD for an optically trapped barium titanate glass (BTG) bead (3.7 μm diameter) in acetone (blue circles; $\tau_p = 11.0$ μs, $\tau_f = 8.5$ μs, $\tau_v = 11.2$ μs), and a silica bead (2.8 μm in diameter) in water (green squares; $\tau_p = 1.2$ μs, $\tau_f = 2.01$ μs, $\tau_v = 0.57$ μs). The red dashed lines indicate the MSD of a particle moving at constant velocity. (**B**) Semilogarithmic plot of the corresponding VACF normalized by $\langle v_{th}^{2*}\rangle \equiv k_B T/m^*$, $(0.18 \text{ mm/s})^2$ and $(0.35 \text{ mm/s})^2$ for the barium titanate and silica microspheres, respectively. The horizontal dashed black line guides the eye to the asymptotic value of the VACF at short times. The solid blue and green lines correspond to the Ornstein-Uhlenbeck model (which neglects hydrodynamic interactions). The dashed red lines correspond to the first-order approximation $1 - \sqrt{t/\tau_v}$. The solid black lines correspond to the full hydrodynamic theory (26).

cumulative velocity spectrum (shown normalized by $\langle v_{th}^{2*} \rangle$ in Fig. 3B), determined by integrating the velocity power spectral density from $\omega = 0$ to $\omega = 2\pi b$. For the filtered velocity to closely approximate the true velocity, b must be high enough to capture most of the area of the velocity power spectrum (Fig. 3A). Because the hydrodynamic velocity spectrum falls off less steeply at high frequency ($\omega^{-3/2}$) than the Ornstein-Uhlenbeck prediction (ω^{-2}), an accurate measurement of
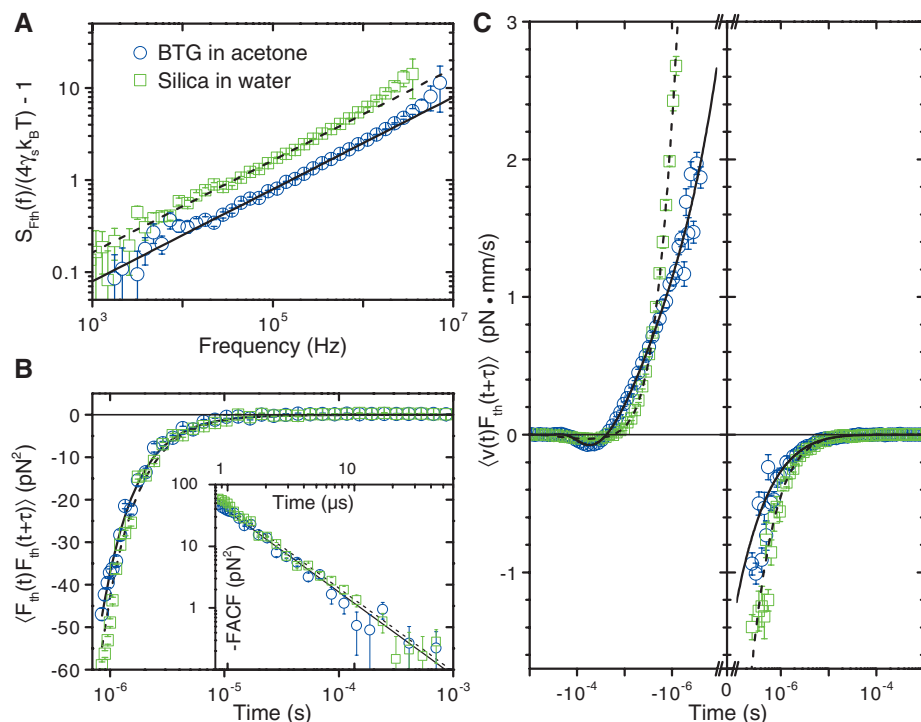
$\langle v_{th}^{2*} \rangle$ requires much higher b than expected from the Ornstein-Uhlenbeck model (22).

Even though the heavier barium titanate bead has lower $\langle v_{th}^{2*} \rangle$, its larger τ_v enables measurement further into the ballistic regime than for the silica microsphere in water. We achieve a noise floor of 2.9 fm/$\sqrt{\text{Hz}}$ in the position spectrum for the silica microsphere in water and 2.1 fm/$\sqrt{\text{Hz}}$ for the barium titanate microsphere in acetone (22), as reflected in fig. S2. Although the noise levels are similar, τ_v is too short to accurately measure the instantaneous velocity of the silica microsphere in water; the noise obscures a substantial fraction of the velocity spectrum. However, for the barium titanate microsphere in acetone, an averaging time of 0.16 μs per velocity sample allows resolution of the instantaneous velocity with a signal-to-noise ratio of ~14 dB. Figure 3C shows the resulting velocity distribution ($v_{rms} = 0.174$ mm/s), as well as that of the velocity noise ($v_{rms} = 34$ μm/s) measured without a bead in the trap but with the same detection power. The velocity distribution is within the experimental uncertainty of the predicted Maxwell-Boltzmann distribution ($v_{rms} = 0.180$ mm/s). The histograms were calculated from 2 million velocity points. The bin size in the velocity histogram was chosen to match the root-mean-square magnitude of the noise. Our measured distribution

corresponds to a mean kinetic energy $0.93\,E_{th}$, to which the noise contributes $0.035\,E_{th}$. A shorter averaging time would increase the fraction of kinetic energy observed at the cost of a lower signal-to-noise ratio.

Although the Ornstein-Uhlenbeck model predicts a thermal force with a white (single-sided) power spectral density of $S_{F_{th}} = 4k_B T \gamma_S$ (16), addition of the Basset term results in a colored component: $S_{F_{th}} = 4k_B T \gamma_S (1 + \sqrt{\omega \tau_f / 2})$ (26). We use the mechanical response corresponding to our fit parameters to infer $F_{th}(t)$ from our recorded trajectories. A log-log plot of $S_{F_{th}}$ with its constant term subtracted reveals the $\sqrt{\omega}$ dependence of the colored component (Fig. 4A). Color in $S_{F_{th}}$ necessarily implies a nondelta autocorrelation function, which we also can observe (Fig. 4B). Interestingly, the force is anticorrelated, displaying a $-3/2$ power-law dependence over our measurement range. Although Stokes damping leads to a delta-correlated thermal force, consisting of uncorrelated "kicks," hydrodynamic coupling effectively adds a negative tail to each kick, which is represented by an additional term $-\gamma_s k_B T \sqrt{\tau_f / 4\pi} \tau^{-3/2}$ in the force autocorrelation.

Measurement of the cross-correlation between the particle's velocity and the nondeterministic, thermal force $C_{vF_{th}}(\tau) \equiv \langle v(t) F_{th}(t+\tau) \rangle$ reveals the causal interplay between the particle

Fig. 3. Analysis of velocity measurements determined from observed Brownian trajectories. (**A**) Double-logarithmic plot of the velocity power spectral density (PSD) and (**B**) semilogarithmic plot of the normalized cumulative velocity PSD for the same particles as in Fig. 2. The solid blue and green lines correspond to the Ornstein-Uhlenbeck model, and the solid black lines correspond to the full hydrodynamic theory (26). The dashed black line guides the eye to the asymptotic approach toward unity. (**C**) The instantaneous-velocity distribution for the barium titanate microsphere in acetone (blue line) and the distribution of the velocity noise (red), both calculated with an averaging time of 0.16 μs. The black line shows the theoretical Maxwell Boltzmann distribution for a temperature of 291 K.

Fig. 4. Statistical properties of thermal force inferred from recorded Brownian trajectories. (**A**) Double-logarithmic plot of the colored component of the thermal force power spectral density for the same particles as in Figs. 2 and 3. (**B**) A semilogarithmic plot of the anticorrelations in the thermal force for the two beads. The inset contains a double-logarithmic plot of the absolute value of the force autocorrelation, showing its power-law dependence. (**C**) Semilogarithmic plot of the cross correlation of the thermal force with the particle velocity. The cross correlation function is asymmetric in time. In all three plots, the black solid and dashed lines correspond to the prediction of the full hydrodynamic theory for the barium titanate and silica microspheres, respectively (26, 27).

and the fluid (Fig. 4C). Unlike autocorrelation, which by definition is time-symmetric, $C_{vF_{th}}(\tau)$ is different for positive and negative τ. The existence of nonzero correlation between the velocity and the thermal force exerted on the bead at future times may seem counterintuitive. This too is a consequence of the hydrodynamic interactions. In the Ornstein-Uhlenbeck model it is exactly zero for τ > 0; the velocity contains no information about future thermal force. Nonzero correlation for positive τ does not violate causality, however. The thermal force of the future is correlated to the thermal force of the past (Fig. 4B), and the velocity is correlated to the thermal force of the past, resulting in nonzero correlation between velocity and the future force (*27*).

Pushing the limits of detection has allowed us to resolve the trajectory in velocity space of Brownian particles in liquid, which, in typical experiments, is normally obscured by noise or concealed by averaging. Our measurements confirm a Maxwell-Boltzmann probability distribution for the velocity with the particle mass replaced by an effective mass that accounts for the inertia of the displaced liquid. Our observations agree with the predicted effects of hydrodynamic interactions on Brownian dynamics, including a faster-than-exponential decay of the VACF and correlations in time of the random thermal force. Our techniques will find broad applications in the study of non-Newtonian fluids (*28*), effects of hydrodynamic interactions in confined geometries (*29*), and nonequilibrium statistical mechanics (*30*, *31*).

References and Notes

1. A. Einstein, *Ann. Phys.* **322**, 549–560 (1905).
2. J. Perrin, *Ann. Chim. Phys.* **18**, 5–104 (1909).
3. M. Kerker, *J. Chem. Educ.* **51**, 764 (1974).
4. A. Einstein, *Zeitschrift für Elektrotechnik und Elektrochemie* **13**, 41–42 (1907).
5. T. Li, S. Kheifets, D. Medellin, M. G. Raizen, *Science* **328**, 1673–1675 (2010).
6. J. Duplat, S. Kheifets, T. Li, M. G. Raizen, E. Villermaux, *Phys. Rev. E* **87**, 020105 (2013).
7. T. Li, S. Kheifets, M. G. Raizen, *Nat. Phys.* **7**, 527–530 (2011).
8. G. L. Paul, P. N. Pusey, *J. Phys. Math. Gen.* **14**, 3301–3327 (1981).
9. R. F. Fox, *J. Math. Phys.* **18**, 2331 (1977).
10. D. A. Beard, T. Schlick, *J. Chem. Phys.* **112**, 7323 (2000).
11. G. Nägele, P. Baur, *Physica A* **245**, 297–336 (1997).
12. H. Craighead, *Nature* **442**, 387–393 (2006).
13. R. Huang *et al.*, *Nat. Phys.* **7**, 576–580 (2011).
14. T. Franosch *et al.*, *Nature* **478**, 85–88 (2011).
15. R. Kubo, *Rep. Prog. Phys.* **29**, 255–284 (1966).
16. G. E. Uhlenbeck, L. S. Ornstein, *Phys. Rev.* **36**, 823–841 (1930).
17. R. Zwanzig, M. Bixon, *J. Fluid Mech.* **69**, 21–25 (1975).
18. J. Boussinesq, *C. R. Hebd. Seances Acad. Sci.* **100**, 935 (1885).
19. A. B. Basset, *Phys. Eng. Sci.* **179**, 43–63 (1888).
20. E. J. Hinch, *J. Fluid Mech.* **72**, 499 (1975).
21. V. Vladimirsky, Y. Terletzky, *Fiz.* **15**, 258–263 (1945).
22. See supplementary materials on *Science* Online.
23. R. Zwanzig, M. Bixon, *Phys. Rev. A* **2**, 2005–2012 (1970).
24. Y. Kim, J. Matta, *Phys. Rev. Lett.* **31**, 208–211 (1973).
25. B. Alder, T. Wainwright, *Phys. Rev. Lett.* **18**, 988–990 (1967).
26. H. J. Clercx, P. P. Schram, *Phys. Rev. A* **46**, 1942–1950 (1992).
27. R. E. London, *J. Chem. Phys.* **66**, 471 (1977).
28. M. Grimm, S. Jeney, T. Franosch, *Soft Matter* **7**, 2076 (2011).
29. B. U. Felderhof, *J. Chem. Phys.* **123**, 184903 (2005).
30. G. M. Wang, E. M. Sevick, E. Mittag, D. J. Searles, D. J. Evans, *Phys. Rev. Lett.* **89**, 050601 (2002).
31. D. Rings, R. Schachoff, M. Selmke, F. Cichos, K. Kroy, *Phys. Rev. Lett.* **105**, 090604 (2010).

Quantum Plasmon Resonances Controlled by Molecular Tunnel Junctions

Shu Fen Tan,[1] Lin Wu,[2] Joel K.W. Yang,[3,4] Ping Bai,*[2] Michel Bosman,*[3] Christian A. Nijhuis*[1,3,5,6]

Quantum tunneling between two plasmonic resonators links nonlinear quantum optics with terahertz nanoelectronics. We describe the direct observation of and control over quantum plasmon resonances at length scales in the range 0.4 to 1.3 nanometers across molecular tunnel junctions made of two plasmonic resonators bridged by self-assembled monolayers (SAMs). The tunnel barrier width and height are controlled by the properties of the molecules. Using electron energy-loss spectroscopy, we directly observe a plasmon mode, the tunneling charge transfer plasmon, whose frequency (ranging from 140 to 245 terahertz) is dependent on the molecules bridging the gaps.

Quantum mechanical effects in plasmonic structures are believed to become important when two plasmonic resonators are placed so closely that electrons can tunnel across the gap (*1–11*). Direct experimental access to the resulting tunneling charge transfer plasmon (tCTP) mode is expected to open up new opportunities in, for instance, nanoscale optoelectronics, single-molecule sensing, and nonlinear optics (*1*). Experimental and theoretical studies so far have concluded that quantum mechanical effects are important only at length scales below 0.3 to 0.5 nm, close to the bond length of gold and silver (*8–11*). Such structures are technologically inaccessible; therefore, it is important to demonstrate the tCTP mode across gaps larger than a nanometer that can be fabricated by state-of-the-art fabrication techniques (*10*). Unlike past works that investigated tunneling through a vacuum (*12*), we placed molecules in the gap because tunneling rates across molecules depend on the molecular structure and are much higher than across a vacuum. This approach made it possible to directly observe and control tCTPs experimentally in tunneling gaps up to at least 1.3 nm, depending on the type of molecules bridging the gap, and to move quantum plasmonics into the size domain that is accessible via bottom-up or top-down fabrication methods (*10*).

Quantum effects have been observed only indirectly as shifts in the bonding dipolar resonance plasmon mode (*1*, *9*, *11*). Our aim was to perform an experiment in which the presence of a tunneling barrier can be directly imaged while the tCTP mode is simultaneously measured spectroscopically by introducing two experimental innovations: The cross-sectional area of the tunnel junction was increased from a few nm² to roughly 10^3 nm², and the tunneling rate across the nanogaps was increased by tunneling through molecules rather than vacuum.

Cuboidal silver nanoparticles were used (*13*), separated by SAMs with thicknesses of 0.5 to 0.6 nm forming metal-SAM-metal junctions through self-assembly (Fig. 1). The facets of the nanoparticles are atomically flat, which results in a very large cross-sectional area of around 10^3 nm², maximizing the number of tunneling events across the junctions. The silver nanoparticles were functionalized with either saturated, aliphatic 1,2-ethanedithiolates (EDT) or aromatic 1,4-benzenedithiolates (BDT) (*14*). The lengths of EDT and BDT are similar, but they have very different HOMO (highest occupied

[1]Department of Chemistry, National University of Singapore, 3 Science Drive 3, Singapore 117543, Singapore. [2]Institute of High Performance Computing, A*STAR (Agency for Science, Technology and Research), 1 Fusionopolis Way, 16-16 Connexis North, Singapore 138632, Singapore. [3]Institute of Materials Research and Engineering, A*STAR, 3 Research Link, Singapore 117602, Singapore. [4]Singapore University of Technology and Design, 20 Dover Drive, Singapore 138682, Singapore. [5]Graphene Research Center, National University of Singapore, 2 Science Drive 3, Singapore 117542, Singapore. [6]Solar Energy Research Institute of Singapore (SERIS), National University of Singapore, Singapore 117574, Singapore.

*Corresponding author. E-mail: baiping@ihpc.a-star.edu.sg (P.B.), michel.bosman@gmail.com (M.B.), christian.nijhuis@nus.edu.sg (C.A.N.)